PAPER

Check for updates

Nanoimprinted conducting nanopillar arrays made of MWCNT/polymer nanocomposites: a study by electrochemical impedance spectroscopy†

Chuan Xiao, [ID] Yuming Zhao [ID] and Wei Zhou [ID] *

Conducting vertical nanopillar arrays can serve as three-dimensional nanostructured electrodes with improved electrical recording and electrochemical sensing performance in bio-electronics applications. However, vertical nanopillar-array electrodes made of inorganic conducting materials by the conventional nanofabrication approach still face challenges in terms of high manufacturing costs, poor scalability, and limited carrier substrates. Here, we report a new type of conducting nanopillar array composed of multi-walled carbon nanotube (MWCNT) doped polymeric nanocomposites, which are manufactured on the wafer-scale on both rigid and flexible substrates by direct nanoimprinting of perfluoropolyether nanowell-array templates into uncured MWCNT/polymer mixtures. By controlling the MWCNT ratios and the annealing temperatures during the fabrication process, MWCNT/polymer nanopillar arrays can be endowed with outstanding electrical properties with high DC conductivity ($\sim$4 S m^{-1}) and low AC electrochemical impedance ($\sim$10^4 Ω at 1000 Hz). Moreover, by electrochemical impedance spectroscopy (EIS) measurements and equivalent circuit modeling analysis, we can decompose the overall impedance of the MWCNT/polymer nanopillar arrays in the electrolyte into multiple bulk and interfacial circuit components, and can thus illustrate their different dependences on the MWCNT ratios and the annealing temperatures. In particular, we find that an appropriate annealing process can significantly reduce the anomalous ion diffusion impedance and improve the MWCNT/ polymer nanopillars' impedance properties in the electrolyte.

1. Introduction

Three-dimensional nanostructured electrodes based on conducting vertical nanopillar arrays have emerged as a useful tool in nano-bioelectronics for electrical recording of extracellular and intracellular membrane potentials[1–5] as well as electrochemical sensing.[6–9] Furthermore, recent studies have shown that living cells can engulf vertical nanopillar electrodes with a tight adhesion to improve electrical coupling at the cell–nanodevice interface.[10,11] Also, dense arrays of nanopillar electrodes can be integrated with large-scale circuits to perform parallel electrical recording over the cellular network.[12] In most previous studies, vertical nanopillar-array electrodes were made of inorganic conducting materials (*e.g.*, Si, Au, and Pt) by conventional nanofabrication techniques using electron-beam lithography and focused ion beam milling, which faces difficulties in terms of high manufacturing costs, poor scalability, and limited choice of carrier substrates. Compared to conventional nanofabrication approaches, nanoimprint lithography

exhibits unique advantages for low-cost scalable nanostructure manufacturing on rigid and flexible substrates.[13–15] Very few studies, however, have been conducted to achieve the scalable nanoimprinting fabrication of conducting nanopillar arrays made of MWCNT/polymer nanocomposites, which can potentially feature appealing properties in terms of combined mechanical flexibility and strength as well as good (bio-)chemical stability and solvent resistance.[16–22]

This work demonstrates the scalable nanoimprinting fabrication of conducting MWCNT/polymer nanopillar arrays, which possess high DC conductivity ($\sim$4 S m^{-1}) and low AC electrochemical impedance ($\sim$10^4 Ω at 1000 Hz). In particular, wafer-scale conducting MWCNT/polymer nanopillar arrays can be manufactured by direct nanoimprinting of perfluoropolyether (PFPE) nanowell-array templates with high stiffness into uncured MWCNT/polymer mixtures. After the curing process, the hydrophobic PFPE nanowell-array templates can be separated from imprinted MWCNT/polymer nanopillar arrays. From 2D Raman mapping measurements, we observe that the distributions of MWCNTs are uniform on the scale of $\sim$25 $\times$ 25 μm^2 but random in the sub-micrometer scale. Furthermore, we conduct 4-point probe DC conductivity measurements and AC electrochemical impedance spectroscopy (EIS) to investigate the effects of the MWCNT ratios and the annealing temperatures on

Department of Electrical and Computer Engineering, Virginia Tech, Blacksburg, VA 24060, USA. E-mail: wzh@vt.edu

† Electronic supplementary information (ESI) available. See DOI: 10.1039/d0na00200c

the electrical properties of MWCNT/polymer nanopillar arrays. By equivalent circuit modeling and analysis, we can decompose the contributions to the overall EIS behaviors from different bulk and interfacial circuit elements. We reveal that the anomalous ion diffusion processes play a significant role in determining the EIS properties of MWCNT/polymer nanopillar arrays in the electrolyte.

2. Experimental

2.1 Materials and chemicals

Carboxyl functionalized MWCNTs with a diameter of 10–20 nm and length of 20–30 μm (purity > 95 wt%) were purchased from Cheap Tubes Inc., USA. The UV-curable polymer NOA83H, also containing the thermal curing catalyst, was supplied by Norland Product Inc., (USA). Sylgard-184 PDMS (Dow Corning) was obtained from Ellsworth Adhesives (USA). PFPE Fluorolink MD 700 was purchased from Solvay S.A. (Belgium). Photoinitiator 2-hydroxy-2-methylpropiophenone was obtained from Sigma-Aldrich (USA). The Silicon 3″ P (100) 0–100 ohm cm SSP 406–480 μm Test Grade wafer was supplied by UniversityWafer Inc. (USA). (Tridecafluoro-1,1,2,2-tetrahydrooctyl)-1-tri (TFCOS) was obtained from UCT Specialties (USA).

2.2 Fabrication of MWCNT/polymer nanopillar arrays

2.2.1 Preparation of uncured MWCNT/NOA83H mixtures. The uncured MWCNT/NOA83H mixtures were created by mixing uncured NOA83H polymer with MWCNT nanofillers at controlled weight percentages using a homogenizer (Fisher Scientific, PowerGen 1000). Mixtures of uncured MWCNT/NOA83H were homogenized by 5 repeating cycles for 1 min at 6000 rpm followed by 1 min rest. We applied 1 min rest between repeating homogenization cycles to alleviate the heating accumulation due to the continuous homogenization process and avoid the undesired partial curing of NOA83H.

2.2.2 Fabrication of polyurethane (PU) nanopillar-array templates. As shown in Fig. 1A, PU nanopillar-array templates were created by nanoimprinting with a PDMS nanowell-array stamp, which was duplicated from a silicon master consisting of a 2D square periodic array of Si nanopillars (periodicity: 400 nm, diameter: ~100 nm, and height: ~400 nm).[23] We conducted the imprinting process with a desktop Compact Imprinting tool (CNI, NIL Technology ApS, Denmark). After dropping 2–3 drops of NOA83H on the PET film (thickness: ~300 μm), the PDMS nanowell-array template was gently placed on the NOA83H droplet to imprint the NOA83H into nanopillar arrays by UV exposure for 5 min (50% power, Fig. S-1†) under 0 bar pressure. A 6 hour post-baking process at 80 °C in an oven was applied to cure the NOA83H-based PU nanopillar-array template fully.

2.2.3 Fabrication of perfluoropolyether (PFPE) nanowell-array templates. PFPE nanowell-array templates were fabricated by nanoimprinting with the TFCOS treated PU nanopillar-array templates (Fig. 1A). After an oxygen plasma surface modification of the PU nanopillar-array templates, the TFCOS treatment was performed in a desiccator for 30 min under

vacuum conditions to make a hydrophobic surface for the PU nanopillar-array templates. The TFOCS treatment of the PU nanopillar arrays will slightly increase their diameter (~10–15 nm on the side) and height (~30 nm) of the nanopillars due to the added TFOCS coating layers (AFM results not shown here).[24] Next, we placed 2–3 drops of PFPE with 4 wt% photoinitiators on the PET film. After placing the PU nanopillar-array template on the PFPE droplet, we loaded the template–PFPE–PET sandwich structures on the CNI nanoimprinting tool for 2 min under 0.5 bar pressure and then conducted UV curing (50% power) for 3 min under 0.5 bar pressure. After peeling off the PU template, we provided additional UV exposure (50% power) for 10 min to cure PFPE nanowell arrays under vacuum (<10 mbar) conditions with suppressed oxygen inhibition of curing processes.

2.2.4 Fabrication of MWCNT/polymer nanopillar arrays. We used the PFPE nanowell-array template to imprint uncured MWCNT/NOA83H mixtures (Fig. 1A) and created conducting nanopillar arrays on both rigid Si substrates (Fig. 1B) and flexible PET films (Fig. 1C). Briefly, Si and PET substrates were cleaned by acetone and IPA rinsing. After drying in a nitrogen flow, we performed oxygen plasma treatment to make the substrate surface hydrophilic in a reactive ion etching system (RIE-1C, Samco, Japan) with an oxygen flow of 20 sccm and RF power of 50 W for 30 s. Next, we placed 2 to 3 drops of uncured MWCNT/NOA83H mixtures on the substrates for the nanoimprinting process. Notably, when the MWCNT filling ratio is above 10 wt%, uncured MWCNT/NOA83H mixtures have a high viscosity to prevent uniform spreading during the imprinting process. To address this issue, we used a blade to evenly spread MWCNT/NOA83H mixtures on the substrates before imprinting. After gently placing the PFPE nanohole-array template on the uncured MWCNT/NOA83H layer, we carried out the imprinting process under suitable pressures (Table S-1†) for ~2 min and then applied UV curing (50% power) for ~10 min with the same pressure. After the imprinting process, we performed an extra thermal curing process of imprinted MWCNT/NOA83H mixtures in an oven at 130 °C for ~150 min.

2.3 Characterization of MWCNT/polymer nanopillar arrays

2.3.1 Raman spectroscopy measurement. We conducted Raman spectroscopy measurements to characterize the distribution of MWCNTs in the fabricated conducting nanopillar-arrays made of MWCNT/polymer composites. A confocal Raman microscope (Alpha 300RS, WITec, Germany) was used to collect Raman signals from 25 × 25 pixels over a 25 × 25 μm² area using a 20× objective lens under 785 nm laser excitation (2 mW) with an integration time of 1 s per pixel. The backscattered photons were detected by a spectrometer (UHTS300, WItec, Germany) equipped with a CCD camera (DU401A, Oxford Instruments, UK). After the signal acquisition, cosmic ray removal and baseline correction were performed using the software Project v4.1 (WITec, Germany).

2.3.2 Four-point probe conductivity characterization. We used a tabletop four-point probe system (Pro4-440N, Sagnatone, USA) to measure the surface conductivity. We used a four-point
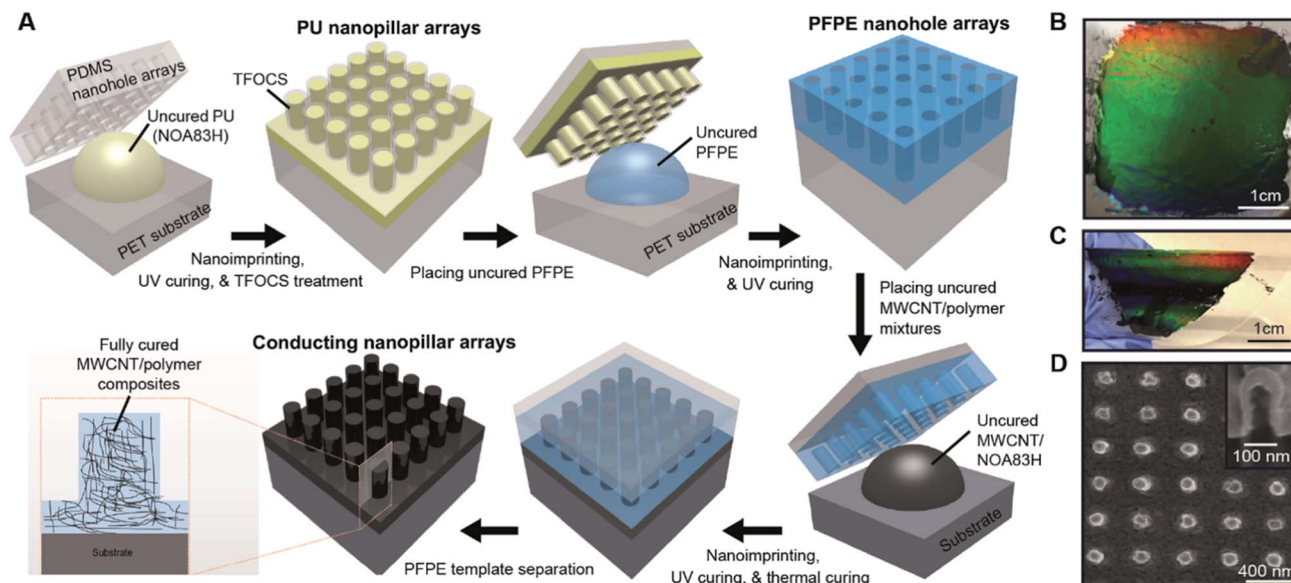
Fig. 1 Nanoimprinting conductive MWCNT/polymer nanocomposite NPAs. (A) Schematic illustration of nanoimprinting fabrication processes to create conductive NPAs of MWCNT/polymer composites by nanoimprinting. (B) Top-down view optical image of conductive MWCNT/polymer composite NPAs on a silicon substrate. (C) Optical image of bent conductive MWCNT/polymer composite NPAs on a flexible PET substrate. (D) Top view and cross-sectional view SEM images of conductive MWCNT/polymer composite NPAs.

resistivity probing head to control the probe–sample interface. The probing head has four probing tips with a radius of 0.04 mm and a tip-to-tip distance of 1.6 mm and uses a pressure of 85 grams during the measurement. For each type of sample, we measured surface conductivity in a total of 20 points from 4 different locations by applying five different voltages. We characterized the thicknesses of the MWCNT/NOA83H composite layers with nanopillar arrays by a profiler (DektakXT, Bruker Corporation, USA), which shows an average thickness of about 40 μm. The conductivity σ was calculated using the expression[25]

$$\sigma = \frac{1}{g} \times \frac{1}{h} \times \frac{V}{I}, \qquad (1)$$

where h is the thickness of the conducting thin film, V is the applied voltage, I is the measured current, and g is the correction factor depending on the geometric parameters in the measurements. In the four-point probe measurements, the distance s between neighboring probes is 0.159 cm, and the thickness h of the imprinted MWCNT/polymer nanopillar array samples is around 40 μm. Since the ratiometric value of h/s (0.0252) is much smaller than 1, the samples can be considered as thin films in the measurements. Considering that the distance of the measured position to the nearest boundary was larger than $5 \times s$ (~0.8 cm), a correction factor g of 4.53 was used to calculate the conductivity.[25]

2.3.3 Electrochemical impedance spectroscopy. We carried out electrochemical impedance spectroscopy (EIS) measurements of conducting nanopillar-array samples between 1 Hz and 100 kHz (10 mV, 10 points per decade) using a portable potentiostat (SP-150, Bio-Logic Science Instruments, USA). The conducting nanopillar-array samples served as the working electrodes and were electrically connected to the potentiostat *via* silver paint and copper wires, which were physically fixed to the surface of conducting nanopillar arrays by the epoxy. PDMS chambers with a 0.5 cm diameter opening were glued with nanopillar-array samples to create electrochemical cells for the EIS measurements with well-defined surface areas of working electrodes. We used a reference electrode (Harvard Apparatus 690023, leak-free reference electrode, 2 mm, Warner Instruments, USA) and a Pt wire counter electrode (99.95% pure, 0.004″ diameter, Surepure Chemicals Inc., USA) for the EIS measurements.

3. Results and discussion

3.1 Fabrication of MWCNT/polymer nanopillar arrays

3.1.1 Nanoimprinting process. As shown in Fig. 1A, we developed a high-throughput fabrication process to manufacture wafer-scale conducting nanopillar arrays by nanoimprinting PFPE nanowell-array templates into uncured MWCNT/polymer mixtures on the planar substrates. With the surface-functionalized carboxyl group, the MWCNTs can achieve a good dispersion quality[19] to blend with the commercially available single-component liquid optical adhesive (NOA-83H) using thiol–ene chemistry, which can allow for both UV curing and thermal curing of the MWCNT/NOA-83H mixture. Notably, the fully cured NOA 83 polymer has shown good biocompatibility and solvent-resistance properties for biological and chemical applications.[18,26] We created PFPE nanowell-array templates on transparent and flexible PET sheets (thickness: ~300 μm) by a two-step replication process, first from a PDMS nanowell-array stamp into a PU nanopillar-array template, and then from a PU nanopillar-array template into a PFPE nanowell-

array template (details in Section 2.2). Compared to nanostructured PDMS templates typically used in the soft lithography process, nanostructured PFPE templates carried on thin PET sheets can provide several advantages for the nanoimprinting fabrication of conducting MWCNT/polymer nanopillar arrays. First, fluoro-polymer based PFPE templates are highly hydrophobic with low surface energy ($\sim$18.5 mN m^{-1}),[17,27] which can ensure their easy separation from imprinted MWCNT/polymer nanopillar arrays after the curing process. Second, PFPE templates have higher stiffness (Young's modulus: $\sim$10.5 MPa) than PDMS templates (Young's modulus: $\sim$2.05 MPa)[17,19] to minimize the deformation of their nanoscale geometries at a high nanoimprinting pressure, which can facilitate accurate molding of nanostructures into uncured MWCNT/polymer mixtures with very high viscosity. Third, our PFPE templates carried on PET thin-sheets are highly flexible/bendable and yet mechanically robust, allowing for conformal contact with substrates of the curved surface and minimizing shear stress during the nanoimprinting process. Since MWCNT nanofillers can efficiently absorb UV light, we purposely used the NOA83H, which can be cured by UV exposure and thermal heating, to create uncured MWCNT/polymer mixtures for the nanoimprinting fabrication of conducting nanopillar arrays. In this way, we can first use the nanoimprinting tool to apply a quick UV curing ($\sim$10 min) to fix the imprinted nanopillar-array nanostructures in the outer layer of uncured MWCNT/polymer mixtures and then use an oven to carry out thermal curing ($\sim$150 min) of MWCNT/polymer mixtures in the inner layer not exposed to UV light for a batch of many samples. Notably, to prevent the oxygen inhibition effect,[28] the UV curing process was performed under vacuum conditions in the camber of the nanoimprinting tool.

3.1.2 **Geometric characterization.** By nanoimprinting, we successfully manufactured wafer-scale MWCNT/polymer nanopillar arrays over a 4 cm $\times$ 4 cm area on both rigid Si substrates (Fig. 1B) and flexible PET polymer sheets (Fig. 1C). From the camera images in Fig. 1B and C, we can observe light diffraction patterns of the rainbow color over large areas from samples, indicating a uniform distribution of periodic nanostructures on the sample surface. The dark appearance in non-diffraction regions reveals a broadband absorption by MWCNT nanofillers at visible frequencies. Fig. 1D shows the top-down and the cross-sectional (the inset of Fig. 1D) scanning electron microscopy (SEM) images of the fabricated MWCNT/polymer nanopillar arrays, which consist of individual vertical nanopillars with a $\sim$100 nm diameter and a $\sim$250 nm height arranged in the square lattice with a 400 nm periodicity.

3.1.3 **Raman characterization of MWCNT distributions.** To investigate the spatial distribution of MWCNTs in the polymer matrix, we performed 2D Raman spectroscopy imaging measurements for the sample of 20 wt% MWCNT/polymer nanopillar arrays under 785 nm laser excitation. As shown in Fig. 2A, the average Raman spectrum from 25 $\times$ 25 pixels exhibits two distinct peaks at $\sim$1340 cm^{-1} and $\sim$1580 cm^{-1} with comparable values of their average peak intensity. The Raman peak at $\sim$1340 cm^{-1} is associated with the disorder-related D-band from the sp^2-hybridized mode of carbon in MWCNTs

mainly due to the carboxyl functionalization group defects on MWCNTs. In comparison, the peak at $\sim$1580 cm^{-1} is the graphene-like G-band from the in-plane mode of carbon atoms in MWCNTs.[29] The 2D confocal Raman image at the D-band (Fig. 2B) and G-band (Fig. 2C) depicts a random distribution of Raman peak intensities without apparent spatial correlation among different pixels. Fig. 2D shows the 2D mapping image of $(I_D + I_G)/2$ obtained by averaging both D-band and G-band Raman intensities to reflect the concentration of randomly oriented MWCNTs at each pixel. Considering a pixel size of 1 μm^2 and a pixel-to-pixel distance of 1 μm, the observation of a random spatial distribution of I_D, I_G, and the $(I_D + I_G)/2$ Raman intensities suggests that the mixing of MWCNT networks is not uniform at the sub-micrometer scale in the polymer matrix. Future research can explore ways to improve the local dispersion uniformity of MWCNT networks in uncured polymer materials, such as using shorter or thinner MWCNTs to reduce the viscosity of MWCNT/polymer mixtures or optimizing the homogenizer tip geometry to improve the mechanical blending efficiency.

For statistical analysis of MWCNT spatial distributions, we plotted the histograms of I_D, I_G, and $(I_D + I_G)/2$ for 25 $\times$ 25 pixels across the 25 μm $\times$ 25 μm area on 20 wt% MWCNT/polymer nanopillar arrays (Fig. 2E), which shows several key points. First, the histogram plots for I_D, I_G, and $(I_D + I_G)/2$ all fit well to the normal distribution shape, indicating that the dispersion of MWCNTs is uniform on the scale of $\sim$25 $\times$ 25 μm^2 despite the significant variations of the MWCNT concentration in the sub-micrometer scale. Second, the I_G histogram shows a larger standard deviation ($\sigma^2 \sim 4.85$) than the I_D histogram ($\sigma^2 \sim 4.38$) since the Raman peak of the in-plane graphene-like G-band in MWCNTs is more sensitive to the orientation variations for MWCNTs than the sp^2-hybridized D-band from localized defects in MWCNTs. Third, the $(I_D + I_G)/2$ histogram shows an even smaller standard deviation ($\sigma^2 \sim 3.28$) by combining the Raman signals from both G-band and D-band contributions, thus providing a better estimation of the local concentrations for MWCNTs of different orientations compared to I_D and I_G.

Considering that I_G from the in-plane G-band is much more sensitive to MWCNT orientations than I_D from the sp^2-hybridized D-band of localized defects, the spatial distribution of the ratiometric I_D/I_G values can reveal the spatial distribution of average MWCNT orientations in the polymer matrix. As shown in Fig. 2F, I_D/I_G values vary widely in the range from 0.1 to 10 with a random spatial distribution, reflecting a random orientation of MWCNTs embedded in MWCNT/polymer nanopillar arrays. Fig. 2G depicts the scatter plot of the relation between I_D and I_G from 25 $\times$ 25 pixels. The broad normal distribution of scatters centered near the position of (10, 10) reveals that the values of I_D and I_G from individual pixels have a relatively weak correlation with each other. Therefore, the spatial distributions of MWCNT concentrations, MWCNT defect densities, and MWCNT orientations are all random, and both I_D and I_G intensities are proportional to MWCNT concentrations.
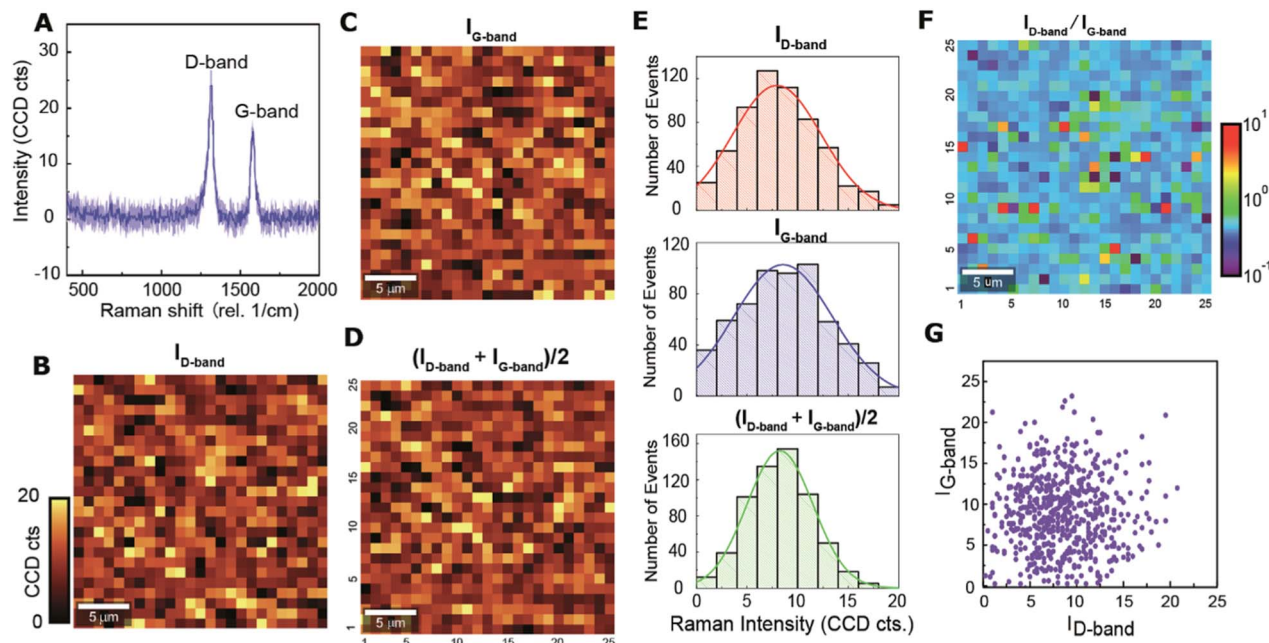
Fig. 2 Raman characterization of conductive MWCNT/polymer composite NPAs. (A) Raman spectra of MWCNTs in a polymer matrix with a 25 × 25 μm area under 785 nm laser excitation. (B–D) Scanning confocal Raman intensity images of MWCNTs in a polymer matrix at (B) I_{D-band} (1340 cm^{-1}), (C) I_{G-band} (1580 cm^{-1}), and (D) $(I_{D-band} + I_{G-band})/2$. (E) Histograms of Raman signal intensities of I_{D-band}, I_{G-band}, and $(I_{D-band} + I_{G-band})/2$. (F) Scanning confocal Raman intensity images of the ratio of I_{D-band}/I_{G-band}. (G) I_{D-band} and I_{G-band} plotting corresponding to each pixel of Raman measurement.

3.2 Study of MWCNT/polymer nanopillar arrays with different MWCNT filling ratios

3.2.1 Conductivity properties. Fig. 3A shows the four-point probe measured conductivity properties for samples of MWCNT/polymer nanopillar arrays with different MWCNT weight ratios. As the MWCNT ratio increases from 0 wt% to 5 wt% and 10 wt%, the conductivity does not change much and only shows small values varying between ~0.0068 S m^{-1} and ~0.0084 S m^{-1}. When the MWCNT ratio increases from 10 wt% to 20 wt%, the samples' conductivity significantly rises from 0.0068 S m^{-1} to 1.99 S m^{-1} by over two orders of magnitude. Thus, a percolation threshold of interconnected MWCNT

networks is reached at an MWCNT weight ratio between 10 wt% and 20 wt%, similar to a previous report.[30] As the MWCNT ratio further increases from 20 wt% to 30 wt%, the samples' conductivity increases from 1.99 to 7.79 S m^{-1} due to the increased density of interconnections in MWCNT networks. The relative standard deviation values of conductivity for 5, 10, 20, and 30 wt% conducting nanopillar arrays are 16.0%, 32.4%, 34.0%, and 9.1%, which can be attributed to spatial variations of MWCNT distributions in the polymer matrix shown in 2D Raman mapping measurements (Fig. 2).

3.2.2 EIS properties. Fig. 3B depicts the EIS measured |Z| spectra in the range between 10^2 Hz and 10^5 Hz for MWCNT/polymer nanopillar arrays with different MWCNT ratios in
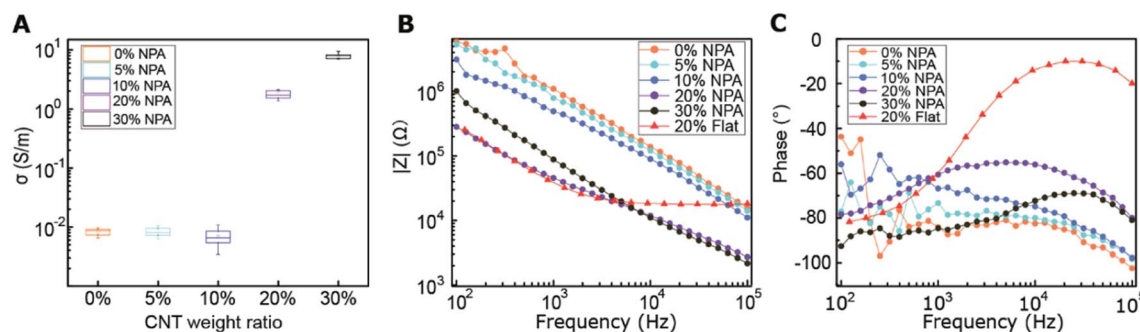
Fig. 3 Conductivity and EIS characterization of different MWCNT ratios of conductive MWCNT/polymer composite. (A) Results of conductivity of 20 points per sample calculated from the sheet resistance measured by 4 point probes of different MWCNT ratios. (B and C) EIS: (B) impedance and (C) phase results of different MWCNT ratios and different conductive MWCNT/polymer composite structures from 10^2 Hz to 10^5 Hz in pH = 7.4 PBS solution.

comparison with a reference sample of 20 wt% MWCNT/polymer flat film. For nanopillar array samples with MWCNT ratios of 0, 5, and 10 wt% below the percolation threshold, their $|Z|$ values continuously decrease from $\sim 3 \times 10^6$ Ω to $\sim 1 \times 10^4$ Ω with increased frequency from 10^2 Hz to 10^5 Hz. In contrast, the $|Z|$ spectra for nanopillar array samples with 20 wt% and 30 wt% MWCNT ratios show significantly reduced values by one order of magnitude over the entire frequency range from 10^2 Hz to 10^5 Hz. Interestingly, the 30% nanopillar array sample shows a slightly lower $|Z|$ than that of the 20% nanopillar array sample at the higher-frequency range (10^4 to 10^5 Hz). However, at the lower-frequency range (10^2 to 10^3 Hz), the 20% nanopillar array sample has a much smaller $|Z|$ than the 30% nanopillar array sample. For example, at 1000 Hz, $|Z|$ for 20 wt% MWCNT/polymer nanopillar arrays is 4.5×10^4 while $|Z|$ for 30 wt% MWCNT/polymer nanopillar arrays is 8.8×10^4 Ω. The observation of a lower impedance for the 20 wt% nanopillar array sample compared to the 30 wt% nanopillar array sample suggests that the 20 wt% nanopillar array sample may have a better dispersion quality of MWCNTs in the polymer matrix due to lower viscosity of uncured MWCNT/polymer mixtures. In contrast, a high MWCNT ratio of 30 wt% may lead to undesired MWCNT aggregation during the blending process, which can reduce the active surface area at the interface with the electrolyte. Compared to 20 wt% MWCNT/polymer nanopillar arrays, the $|Z|$ spectrum for the 20 wt% MWCNT/polymer flat film shows a similar shape of decreasing $|Z|$ values with the frequency increased from $\sim 1 \times 10^2$ Hz to $\sim 3 \times 10^3$ Hz. However, as the frequency further increases from $\sim 3 \times 10^3$ Hz to $\sim 1 \times 10^5$ Hz, the $|Z|$ values of the flat MWCNT/polymer sample start to level off around 1.7×10^4 Ω, indicating that the impedance properties of MWCNT/polymer composites also depend on the nanostructured surface geometries.

Fig. 3C shows the spectra of the impedance phase angle for different MWCNT/polymer samples. For nanopillar array samples with 0, 5, and 10 wt% MWCNT ratios, as the frequency decreases from $\sim 10^5$ Hz to $\sim 10^3$ Hz, the impedance phase angle first increases and then slowly levels off; as the frequency further decreases from $\sim 10^3$ Hz to $\sim 10^2$ Hz, the impedance phase angle starts to fluctuate significantly in a random manner due to the longer travel distance of ions at the lower frequency range. For the nanopillar array with 20 wt% MWCNT ratio, as the frequency increases from $\sim 10^2$ Hz to $\sim 10^4$ Hz, the impedance phase angle increases from $\sim -80°$ to the peak value of $\sim -55°$, and as the frequency further increases to $\sim 10^5$ Hz, the phase angle reduces to $\sim -81°$. Unlike the 20 wt% MWCNT/polymer nanopillar arrays, 30 wt% MWCNT/polymer nanopillar arrays show a peak impedance phase angle of $\sim -70°$ at $\sim 2 \times 10^4$ Hz, and the flat MWCNT/polymer sample shows a peak impedance phase angle of $\sim -10°$ at $\sim 1 \times 10^4$ Hz.

3.2.3 Analysis by equivalent circuit modeling. To better understand the effects of MWCNT ratios and nanostructured surface geometries on EIS properties, we conducted an equivalent circuit modeling to fit and analyze the measured Nyquist plots for different MWCNT/polymer samples. Fig. 4A illustrates the equivalent circuit we used for fitting the EIS spectra, where R'_1 is the electrolyte resistance, R''_1 is the bulk resistance

of the MWCNT/polymer composite, R'''_1 includes all parasitic contact resistance and equipment resistance in the circuit, C''_1 describes the bulk capacitance of the MWCNT/polymer composite, R_2 is the charge transfer resistance at the interface between MWCNTs and the electrolyte, C_2 is the double-layer capacitance at the interface between MWCNTs and the electrolyte, and Ma_3 is the anomalous diffusion impedance for ion diffusion at the interface between MWCNTs and the electrolyte. In particular, the anomalous diffusion of ions is mainly caused by the nanoscale porous structures at the interface between MWCNT/polymer composites and the electrolyte.[31,32] The diffusion of ions in the porous structure does not obey Fick's laws and thus cannot be modeled as a standard Warburg impedance term. By modifying Fick's equations and solving the differential equations under nanoporous boundary conditions, the anomalous diffusion impedance Ma_3 can be expressed as[33]

$$Ma_3(j\omega) = Rd_3 \times \left(\frac{\omega_d}{j\omega}\right)^{\alpha/2} \times \coth\left[\left(\frac{j\omega}{\omega_d}\right)^{\alpha/2}\right], \quad (2)$$

$$\frac{2\pi}{\omega_d} = \frac{t^2}{D}, \quad (3)$$

where Rd_3 is the anomalous diffusion impedance amplitude, j is the imaginary unit, ω is the frequency, ω_d is the characteristic angular frequency, α is the sub-diffusion parameter for describing the fractal geometry of nanoporous structures, t is the effective thickness of the nanoporous MWCNT/polymer layer for the anomalous diffusion, and D is the diffusion coefficient. The ion movement behaviors are very different between low-frequency and high-frequency limits. When ω is much larger than ω_d, the effective ion concentration at the electrode surface is not disturbed by AC electrical fields, reaching the chemical dynamics regime. When ω is much smaller than ω_d, the ion concentration at the electrode surface depends on the phase of AC electrical fields and the ion diffusion constant, reaching the diffusion regime.

Fig. 4B depicts the Nyquist plots in the range between 10^3 and 10^5 Hz for different MWCNT/polymer samples. Based on the equivalent circuit modeling in Fig. 4A, we used the randomization method to fit equivalent circuit elements and produced fitting curves (dashed lines, Fig. 4B) in good agreement with measurements (discrete dots, Fig. 4B) for different samples. The randomization fitting methods start with some initial parameter values and randomize them to minimize $\chi^2/|Z|$ in ohm. $\chi^2/|Z|$ can be expressed as[34]

$$\chi^2/|Z| = \frac{1}{n}\sum_{i=1}^{n}\frac{|Z_{meas}(i) - Z_{simul}(\omega_i, param)|^2}{(Z_{meas}(i))}, \quad (4)$$

where $Z_{meas}(i)$ is the measured impedance, and $Z_{simul}(\omega_i, param)$ is the calculated value based on fitting parameters at different frequencies ω_i. By examining the fitted values of the equivalent circuit elements in Table 1, we can have a mechanistic understanding of the difference in EIS properties between different samples. Since R''_1 resistance for the MWCNT/polymer sample is in series with the electrolyte resistance R'_1 and the remaining
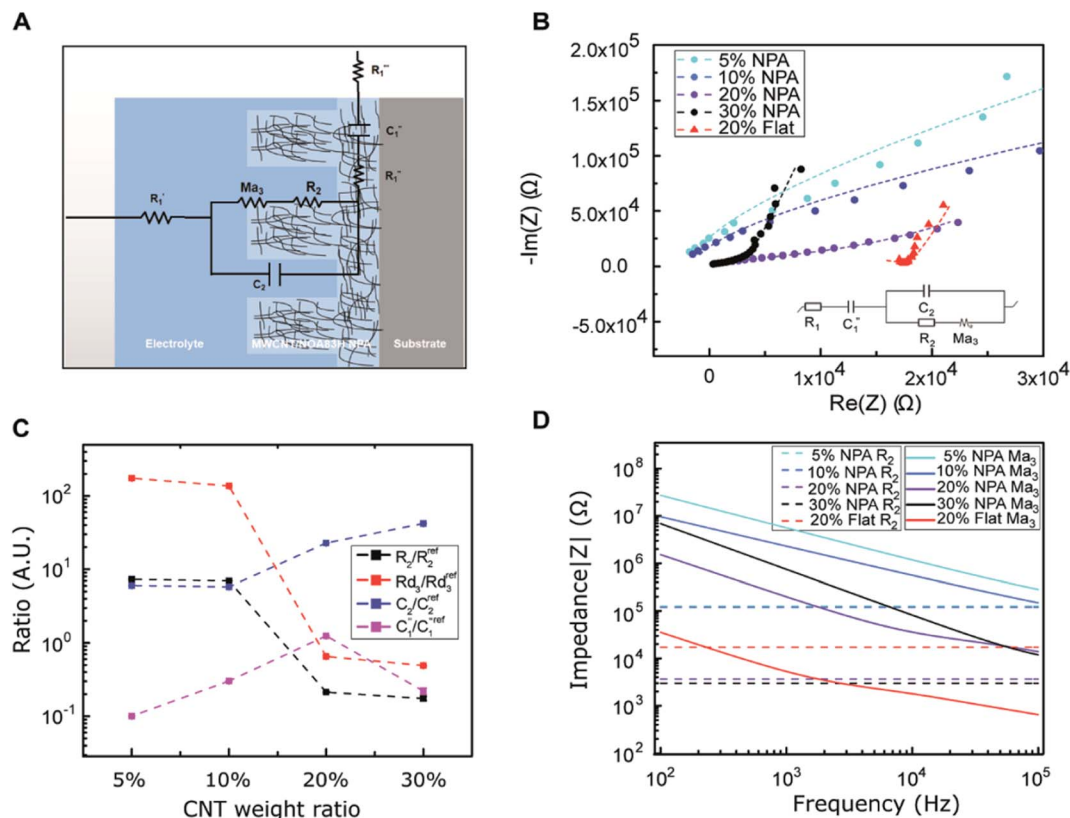
Fig. 4 Analysis of different MWCNT ratios of conductive MWCNT/polymer composites. (A) Schematic equivalent circuit model. (B) Nyquist plots and equivalent circuit models of different MWCNT ratios and different conductive MWCNT/polymer composite structures from 10^2 Hz to 10^5 Hz in pH = 7.4 PBS solution. (C) The ratio plot of different fitting parameters to the conductive MWCNT/polymer flat composite reference for different MWCNT loadings of conductive MWCNT/polymer composites. (D) The plot of R_2 and calculated Ma_3 value of different MWCNT ratios and different structures of the conductive MWCNT/polymer composite from 10^2 Hz to 10^5 Hz.

parasitic circuit/contact resistance R'''_1, R''_1 cannot be differentiated from R'_1 and R'''_1 in the fitting. Thus, the table does not include the circuit items for R'_1, R''_1, and R'''_1.

As shown in Table 1, the 20 wt% MWCNT/polymer flat sample and the 20 wt% MWCNT/polymer nanopillar arrays share similar fitted values of anomalous diffusion impedance (including Rd_3, t_3, and α_3) and MWCNT network capacitance (C''_1), indicating their similar fractal nanoporous structures as well as similar distribution and density properties of MWCNT networks. However, 20 wt% MWCNT/polymer nanopillar arrays show much smaller values for both charge transfer resistance (R_2: ~3653 Ω) and double-layer capacitance (C_2: ~0.618 × 10^{-9} F) than the 20 wt% MWCNT/polymer flat sample (R_2: ~17 127

Ω, C_2: ~2.712 × 10^{-11} F), reflecting the much larger active surface area to interact with the electrolyte environment in both faradaic and non-faradaic processes. The observation of very different R_2 and C_2 values between nanopillar array and flat samples of the same 20% MWCNT ratio suggests that the nanoimprinting process for creating nanopillar arrays may mechanically force more MWCNTs to penetrate out of their polymer matrix for direct interfacing with electrolytes. The impedance of a capacitor inversely depends on the frequency and can be expressed as

$$Z_c = \frac{1}{\omega C}j, \tag{5}$$

Table 1 Fitting parameters of different MWCNT ratios

Condition	Circuit components						
	$\chi^2/|Z|$	R_2 (Ω)	Rd_3 (Ω)	Wd_3 (rad s^{-1})	a_3 (a.u.)	C_2 (nF)	C''_1 (F)
20% flat	0.43	17 127	3.43×10^6	0.061	0.999	2.712×10^{-2}	5.38
5% NPA	0.358	125 428	5.94×10^8	0.050	0.989	0.164	0.54
10% NPA	0.267	119 300	4.67×10^8	0.057	0.995	0.157	1.62
20% NPA	0.052	3654	2.22×10^6	0.070	0.806	0.618	6.71
30% NPA	0.031	3985	1.67×10^6	0.085	0.885	1.141	1.18

$$C = \varepsilon \frac{A}{d}, \qquad (6)$$

where C is the capacitance, ε is the permittivity, A is the area of the two neighboring electrodes, and d is the distance between the two neighboring electrodes. For the 20 wt% MWCNT/polymer flat sample, at 10^5 Hz, the $|Z_{C_2}|$ calculated using eqn (5) is 58 946 Ω, and the $|\text{Ma}_3|$ calculated using eqn (2) is 649.94 Ω. Therefore, $|Z_{C_2}|$ is much larger than the summation of R_2 and $|\text{Ma}_3|$, which explains its frequency-insensitive impedance response between $\sim 3 \times 10^3$ Hz and $\sim 1 \times 10^5$ Hz (Fig. 3B). In contrast, for 20 wt% MWCNT/polymer nanopillar arrays at 10^5 Hz, $|Z_{C_2}|$ is 9705 Ω, $|\text{Ma}_3|$ is 13 882 Ω, and R_2 is 3653 Ω. Since $|Z_{C_2}|$ is smaller than the summation of R_2 and $|\text{Ma}_3|$, the impedance for 20 wt% MWCNT/polymer nanopillar arrays continuously decreases with increasing frequency (Fig. 3B).

To examine the effects of the MWCNT ratio on the electrochemical impedance properties for nanopillar arrays, we used the 20 wt% MWCNT/polymer flat sample as a reference to plot the fitted ratiometric values of equivalent circuit elements, including $C''_1/C''^{(\text{ref})}_1$ for the MWCNT network capacitance, $C_2/C^{(\text{ref})}_2$ for the double-layer capacitance, $R_2/R^{(\text{ref})}_2$ for the charge transfer resistance, and $\text{Rd}_3/\text{Rd}^{(\text{ref})}_3$ for the anomalous diffusion impedance. In Fig. 4C, we can observe several key points. First, before reaching the percolation threshold, as the MWCNT ratio increases from 5 wt% to 10 wt%, $C''_1/C''^{(\text{ref})}_1$ increases from 0.10 to 0.30 by ~ 3 times, $C_2/C^{(\text{ref})}_2$ slightly increases from 6.05 to 5.79, $R_2/R''^{(\text{ref})}_2$ slightly decreases from 7.32 to 6.97, and $\text{Rd}_3/\text{Rd}''^{(\text{ref})}_3$ decreases from 174.70 to 137.35. Therefore, for the disconnected MWCNTs in the polymer matrix, the change of MWCNT ratios does not significantly affect the values for the circuit elements at the interface with electrolyte environments (e.g., C_2, R_2, and Rd_3). However, the bulk capacitance C''_1 can still increase significantly with the MWCNT ratio due to an increased electrode surface area (A) of MWCNTs and a reduced mean distance (d) between MWCNTs in the MWCNT/polymer composite, described by eqn (6). Second, as the MWCNT ratio increases from 10 wt% to 20 wt% across the percolation threshold, $C''_1/C''^{(\text{ref})}_1$ increases from 0.30 to 1.25, $C_2/C^{(\text{ref})}_2$ increases from 5.8 to 22.8 by ~ 4 times, $R_2/R''^{(\text{ref})}_2$ decreases from 6.97 to 0.21, and $\text{Rd}_3/\text{Rd}''^{(\text{ref})}_3$ decreases from 137.4 to 0.65. In addition to the ~ 4 times increase of interfacial and bulk capacitance C''_1 and C_2, reaching the percolation threshold can lead to a ~ 35 times drop of R_2 and a ~ 210 times drop of Rd_3, which suggests that the charge transport and ion diffusion processes at the electrolyte interface strongly depend on the formation of interconnected MWCNT networks. Third, after going beyond the percolation threshold, as the MWCNT ratio further increases from 20% to 30%, $C''_1/C''^{(\text{ref})}_1$ decreases from 1.25 to 0.22 by ~ 5.7 times, $C_2/C^{(\text{ref})}_2$ increases from 22.78 to 42.07 by ~ 2 times, $R_2/R''^{(\text{ref})}_2$ slightly decreases from 0.21 to 0.17, and $\text{Rd}_3/\text{Rd}''^{(\text{ref})}_3$ slightly decreases from 0.65 to 0.49. The significant drop for the bulk capacitance C''_1 and relatively small changes for interfacial circuit elements of C_2, R_2, and Rd_3 can be explained by the formation of MWCNT aggregations in the polymer matrix because of the poor dispersion of MWCNTs in the polymer matrix at very high MWCNT ratios ($\sim 30\%$).

To investigate the relative contributions to the interfacial impedance between the charge transport term R_2 and ion diffusion term Ma_3, we compared the fitted impedance spectra for R_2 (solid curves, Fig. 4D) and Ma_3 (solid curves, Fig. 4D) for different samples. Unlike R_2 which is independent of frequency changes, the impedance for Ma_3 decreases with the frequency following eqn (2). Compared to the 20% MWCNT/polymer flat sample, the 20% MWCNT/polymer nanopillar arrays show a ~ 45 times impedance increase for Ma_3 but a ~ 5 times impedance drop for R_2 over the entire frequency range between 10^2 and 10^5 Hz (Fig. 4D). The smaller R_2 for the nanopillar sample than the flat sample suggests that the mechanical forces during the nanostructured imprinting process can expose more electrochemically active MWCNTs on the surface of MWCNT/polymer nanopillar arrays in the electrolyte environment. On the other hand, the much larger Ma_3 impedance for the nanopillar sample than the flat sample indicates that the nanoimprinting process can cause a higher degree of microscopic porosity on the surface of MWCNT/polymer nanopillar arrays to slow down the ion diffusion process at the interface with the electrolyte. For MWCNT/polymer nanopillar arrays with different MWCNT ratios, the impedance for Ma_3 is dominant over R_2 (Fig. 4D), revealing a faster rate of the faradaic electron charge transport process than the ion diffusion process in the tested frequency range between 10^2 and 10^5 Hz.

To access the sample uniformity in terms of EIS properties and the fabrication process reproducibility, we carried out EIS measurements at three different spots for each sample and three samples under each of the processing conditions (Fig. S-4, ESI†). We further fitted the EIS measurement results with the equivalent circuit model in Nyquist plots (Fig. S-5, ESI†). The fitted parameters show similar values (Table S-2, ESI†) between different spots on the same samples and between different samples under the same processing conditions, manifesting good sample uniformity and good fabrication reproducibility for making MWCNT/polymer NPAs.

3.3 Study of MWCNT/polymer nanopillar arrays with different annealing temperatures

3.3.1 Conductivity properties. We investigated the annealing effects on the electrical properties of 20 wt% MWCNT/polymer nanopillar arrays by 4-point probe measurements. As the annealing temperature increases from 130 °C to 200 °C and 300 °C, the sample's conductivity increases from 3.58 S m^{-1} to 5.99 S m^{-1} and 6.41 S m^{-1}, and the relative standard deviation increases from 34.0% to 65.5% and 95.8% (Fig. 5A). The observation of increased conductivity with the annealing temperature for MWCNT/polymer nanopillar arrays indicates that the annealing process can increase the MWCNT networks' connectivity in the polymer matrix. As suggested by previous reports,[35,36] with the annealing temperature above the polymer glass transition temperature, the nanoimprinting-stressed MWCNTs can experience self-relaxation and self-reorientation in the softened polymer matrix, which may reduce the mean distance among individual MWCNTs in the network to increase the conductivity of MWCNT networks. The increase of the
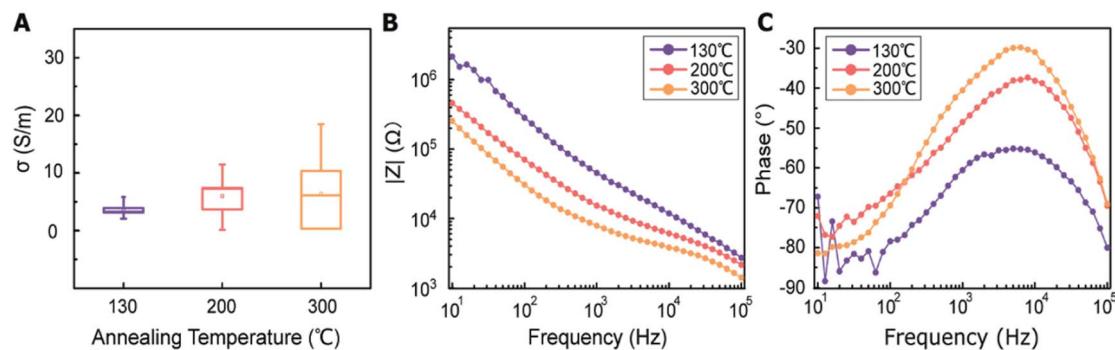
Fig. 5 Conductivity and EIS characterization of annealing effect on 20 wt% conductive MWCNT/polymer composite NPAs. (A) Results of conductivity of 20 points per sample calculated from the sheet resistance measured by a 4 point probe of the annealing effect on a 20 wt% conductive MWCNT/polymer composite. (B and C) EIS: (B) impedance and (C) phase results of different annealing effects on the 20 wt% conductive MWCNT/polymer composite from 10^1 Hz to 10^5 Hz in pH = 7.4 PBS solution.

relative standard deviation of measured conductivity with increased annealing temperature may be associated with the stochastic nature of self-relaxation and self-reorientation processes of MWCNT networks, which are non-uniformly distributed in the polymer matrix. Notably, we have observed that the nanopillar structure of MWCNT/polymer can vanish at annealing temperatures above 400 °C.

3.3.2 EIS properties. Fig. 5B shows that MWCNT/polymer nanopillar arrays treated at higher annealing temperatures possess a lower impedance over the tested frequency range between 10^2 and 10^5 Hz. At 1000 Hz, as the annealing temperature increases from 130 °C to 200 °C and 300 °C, the impedance drops from 4.5×10^4 Ω to 1.5×10^4 Ω and 7.9×10^3 Ω, which agrees with the decreasing trend of measured DC conductivity (Fig. 5A). As shown in Fig. 5C, conductive nanopillar arrays with different annealing temperatures reveal a similar profile for measured spectra of impedance phase angle, which first increases and then decreases with frequency, reaching a peak value between 10^3 Hz and 10^4 Hz.

3.3.3 Analysis by equivalent circuit modeling. To understand the EIS properties of MWCNT/polymer nanopillar arrays under different annealing temperatures, we conducted equivalent circuit modeling (Fig. 4A) to fit the measured curves in the Nyquist plot (Fig. 6A). Table 2 illustrates the fitted parameters of the circuit elements for different samples. By using the 20 wt% MWCNT/polymer flat sample as a reference, we plotted the ratiometric values of $C''_1/C''^{(\text{ref})}_1$, $C_2/C^{(\text{ref})}_2$, $R_2/R^{(\text{ref})}_2$, and $\text{Rd}_3/\text{Rd}^{(\text{ref})}_3$ for 20 wt% MWCNT/polymer nanopillar arrays with different annealing temperatures (Fig. 6B).

As the annealing temperature increases from 130 °C to 200 °C, $C''_1/C''^{(\text{ref})}_1$ increases by ∼5 times from 1.25 to 7.51, $\text{Rd}_3/\text{Rd}''^{(\text{ref})}_3$ decreases from 0.65 to 0.46, $C_2/C^{(\text{ref})}_2$ slightly increases from 22.79 to 25.40, and $R_2/R''^{(\text{ref})}_2$ slightly changes from 0.21 to 0.20 (Fig. 6B). The significant increase of the bulk capacitance term $C''_1/C''^{(\text{ref})}_1$ indicates a reduced mean distance (d) between individual MWCNTs due to the self-relaxation and self-reorientation of MWCNTs in the softened polymer matrix at 200 °C, which agrees with the observation of increased conductivity from 4-probe measurements (Fig. 5A). The decrease of the anomalous diffusion term $\text{Rd}_3/\text{Rd}''^{(\text{ref})}_3$ suggests a reduced nanoscale porosity at the interface between MWCNT/ polymer nanopillar arrays and the electrolyte due to the
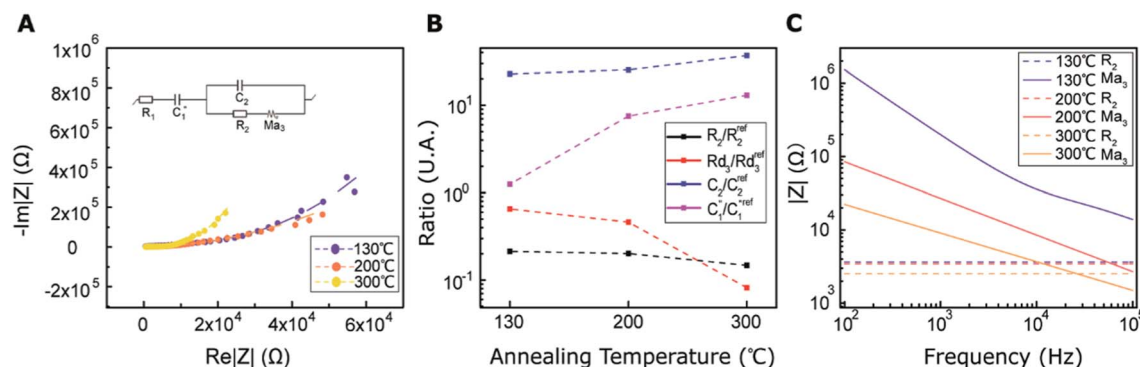

Fig. 6 Analysis of the annealing effect on conductive MWCNT/polymer composite NPAs. (A) Nyquist plots and equivalent circuit model of conductive MWCNT/polymer composite NPAs with different annealing temperatures from 10^2 Hz to 10^5 Hz. (B) The ratio plot of different fitting parameters to the conductive MWCNT/polymer flat composite reference for different annealing temperatures on conductive MWCNT/polymer composite NPAs. (C) The plot of R_2 and calculated Ma_3 value of different annealing temperatures on conductive MWCNT/polymer composite NPAs from 10^2 Hz to 10^5 Hz.

Table 2 Fitting parameters of the annealing effect on conducting nanopillar arrays

Condition	Circuit components						
	$\chi^2/|Z|$	R_2 (Ω)	Rd_3 (Ω)	Wd_3 (rad s^{-1})	a_3 (a.u.)	C_2 (nF)	C''_1 (F)
20% NPA 0 °C	0.052	3653	2.22×10^6	0.070	0.806	0.618	6.716
20% NPA 200 °C	0.035	3451	1.57×10^6	0.145	0.792	0.683	40.43
20% NPA 300 °C	0.032	2525	2.78×10^5	0.995	0.782	1.032	70.08

annealing. The small changes of the double-layer capacitance term $C_2/C_2^{(ref)}$ and charge transport resistance term $R_2/R''_2^{(ref)}$ indicate that the density of the interfacial MWCNTs exposed to the electrolyte does not change much with the annealing temperature increased from 130 °C to 200 °C.

As the annealing temperature further increases from 200 °C to 300 °C, $C''_1/C''_1^{(ref)}$ increases from 7.51 to 13.02, $Rd_3/Rd''_3^{(ref)}$ decreases by ∼6 times from 0.46 to 0.08, $C_2/C_2^{(ref)}$ increases from 25.40 to 36.87, and $R_2/R''_2^{(ref)}$ decreases from 0.20 to 0.15 (Fig. 6B). Therefore, by using an even higher annealing temperature at 300 °C, the mean distance between individual MWCNTs can be further decreased to increase the bulk capacitance term $C''_1/C''_1^{(ref)}$, and the nanoscale porosity can also be reduced to decrease the ion diffusion impedance $Rd_3/Rd''_3^{(ref)}$. Furthermore, the significant increase of the double-layer capacitance term $C_2/C_2^{(ref)}$ and non-negligible decrease of the charge transport resistance term $R_2/R''_2^{(ref)}$ suggest an increased density of the interfacial MWCNTs exposed to the electrolyte, which may be due to the heat-induced rearrangement of the interfacial MWCNTs on the surface of MWCNT/polymer nanopillar arrays.

Fig. 6C compares the interfacial impedance contributions due to the charge transport term R_2 and the anomalous ion diffusion term Ma_3 for MWCNT/polymer nanopillar arrays with different annealing temperatures. First, by increasing the annealing temperature from 130 °C to 200 °C and 300 °C, the impedance for anomalous ion diffusion Ma_3 can decrease by almost 2 orders of magnitude in the frequency range between 10^2 and 10^5 Hz, while the charge transport resistance R_2 decreases by a much smaller factor. Second, although the impedance for Ma_3 is dominant over R_2 in the frequency range below 10^4 Hz, the difference of the impedance values between Ma_3 and R_2 can be significantly reduced by the annealing process at 300 °C. Therefore, an appropriate annealing process can help to reduce the overall impedance of MWCNT/polymer nanopillar arrays in (1) the bulk contributions from the resistance R''_1 and capacitance C''_1 terms of MWCNT networks by softening the polymer matrix and reducing the mean distance between MWCNTs, (2) as well as the interfacial contributions from the anomalous ion diffusion Ma_3 and charge transport R_2 terms by smoothing the nanoporous structures and increasing the MWCNT densities exposed to the electrolyte.

conducting MWCNT/polymer nanopillar arrays on the wafer-scale on both rigid and flexible substrates. We have conducted a systematic study to characterize and understand the dependence of the electrical properties of MWCNT/polymer nanopillar arrays on the MWCNT ratios and the annealing temperatures in the fabrication process. In particular, we find that both charge transport resistance and anomalous ion diffusion impedance at the electrolyte interface can decrease dramatically by increasing the MWCNT ratio over the percolation threshold to form interconnected MWCNT networks. Furthermore, we observe that MWCNT/polymer nanopillar arrays treated at annealing temperatures of 200 and 300 °C can have increased bulk conductivity, increased bulk capacitance, and reduced interfacial anomalous ion diffusion impedance. Compared to most nanopillar arrays made of inorganic conducting materials (e.g., Si, Au, and Pt) by conventional nano-engineering, nanoimprinting fabricated conducting MWCNT/polymer nanopillar arrays have unique advantages, such as combined mechanical flexibility and strength, roll-to-roll manufacturing scalability, and fabrication compatibility with both rigid and flexible substrates. Therefore, we envision that conducting MWCNT/polymer nanopillar arrays obtained by scalable nanoimprinting fabrication can open new opportunities in flexible wearable sensing devices, flexible implantable biosensors, and low-cost disposable biochips. Toward the use of conducting MWCNT/polymer nanopillar arrays for bioelectrical recording and electrochemical sensing, future research can explore the methods (1) for further improvement of the local dispersion uniformity of MWCNT networks in uncured polymer materials and (2) for scalable patterning, metallization, lift-off, and passivation processes to create many individually addressable recording sites composed of MWCNT/polymer nanopillar arrays.

Conflicts of interest

There are no conflicts to declare.

Acknowledgements

4. Conclusion

In summary, we have developed a scalable, low cost, and high throughput nanoimprinting fabrication process to manufacture

References

1 L. Hanson, Z. C. Lin, C. Xie, Y. Cui and B. X. Cui, Nano Lett., 2012, 12, 5815–5820.

2 J. T. Robinson, M. Jorgolli, A. K. Shalek, M. H. Yoon, R. S. Gertner and H. Park, *Nat. Nanotechnol.*, 2012, **7**, 180–184.

3 C. Xie, Z. L. Lin, L. Hanson, Y. Cui and B. X. Cui, *Nat. Nanotechnol.*, 2012, **7**, 185–190.

4 Z. L. C. Lin, C. Xie, Y. Osakada, Y. Cui and B. X. Cui, *Nat. Commun.*, 2014, **5**, 3206.

5 J. Abbott, T. Y. Ye, L. Qin, M. Jorgolli, R. S. Gertner, D. Ham and H. Park, *Nat. Nanotechnol.*, 2017, **12**, 460–466.

6 C. Shin, W. Shin and H. G. Hong, *Electrochim. Acta*, 2007, **53**, 720–728.

7 F. J. Rawson, M. T. Cole, J. M. Hicks, J. W. Aylott, W. I. Milne, C. M. Collins, S. K. Jackson, N. J. Silman and P. M. Mendes, *Sci. Rep.*, 2016, **6**, 37672.

8 M. Yang, S. B. Hong, J. H. Yoon, D. S. Kim, S. W. Jeong, D. E. Yoo, T. J. Lee, K. G. Lee, S. J. Lee and B. G. Choi, *ACS Appl. Mater. Interfaces*, 2016, **8**, 22220–22226.

9 C. Lotwala and H. F. Ji, *AIMS Mater. Sci.*, 2017, **4**, 292–301.

10 W. T. Zhao, L. Hanson, H. Y. Lou, M. Akamatsu, P. D. Chowdary, F. Santoro, J. R. Marks, A. Grassart, D. G. Drubin, Y. Cui and B. X. Cui, *Nat. Nanotechnol.*, 2017, **12**, 750–756.

11 H. Y. Lou, W. T. Zhao, Y. P. Zeng and B. X. Cui, *Acc. Chem. Res.*, 2018, **51**, 1046–1053.

12 J. T. Robinson, M. Jorgolli, A. K. Shalek, M.-H. Yoon, R. S. Gertner and H. Park, *Nat. Nanotechnol.*, 2012, **7**, 180–184.

13 K. J. Byeon and H. Lee, *Eur. Phys. J.: Appl. Phys.*, 2012, **59**, 10001.

14 L. J. Guo, *Adv. Mater.*, 2007, **19**, 495–513.

15 M. C. Traub, W. Longsine and V. N. Truskett, *Annu. Rev. Chem. Biomol. Eng.*, 2016, **7**, 583–604.

16 J. Yu, K. Lu, E. Sourty, N. Grossiord, C. E. Koning and J. Loos, *Carbon*, 2007, **45**, 2897–2903.

17 J. Fawaz, and V. Mittal, Polymer Nanotube Nanocomposite: A Review of Synthesis Methods, Properties and Applications, *Polymer Nanotube Nanocomposites: Synthesis, Properties, and Applications*, MA: Scrivener Publishing LLC, 2nd edn, 2014, pp. 25–27.

18 T. D. Prichard, S. S. Singh, N. Chawla and B. D. Vogt, *Polymer*, 2013, **54**, 1130–1135.

19 S. Kundu, Y. Wang, W. Xia and M. Muhler, *J. Phys. Chem. C*, 2008, **112**, 16869–16878.

20 Y. Guo, K. Ruan, X. Yang, T. Ma, J. Kong, N. Wu, J. Zhang, J. Gu and Z. Guo, *J. Mater. Chem. C*, 2019, **7**, 7035–7044.

21 A. Forcellese, M. Simoncini, A. Vita, A. Giovannelli and L. Leonardi, *J. Mater. Process. Technol.*, 2020, **286**, 116839.

22 M. Kumar, J. S. Saini and H. Bhunia, *J. Mater. Eng. Perform.*, 2020, **29**, 7511–7525.

23 J. Henzie, M. H. Lee and T. W. Odom, *Nat. Nanotechnol.*, 2007, **2**, 549–554.

24 B. Bhushan, D. Hansford and K. K. Lee, *J. Vac. Sci. Technol., A*, 2006, **24**, 1197–1202.

25 B. Technology, *Four Point Probe Equations*, http://four-point-probes.com/four-point-probe-equations/.

26 E. P. Dupont, R. Luisier and M. A. M. Gijs, *Microelectron. Eng.*, 2010, **87**, 1253–1255.

27 D. Qin, Y. Xia and G. M. Whitesides, *Nat. Protoc.*, 2010, **5**, 491.

28 J.-D. Cho, D.-P. Kim and J.-W. Hong, *Open J. Org. Polym. Mater.*, 2014, **04**(No. 01), 4.

29 L. Bokobza and J. Zhang, *eXPRESS Polym. Lett.*, 2012, **6**, 601–608.

30 F. Du, J. E. Fischer and K. I. Winey, *Phys. Rev. B: Condens. Matter Mater. Phys.*, 2005, **72**, 121404.

31 Z. Pomerantz, G. Garcia-Belmonte, A. Joseph, J.-P. Lellouche, J. Bisquert and A. Zaban, *Electrochim. Acta*, 2007, **52**, 6841–6847.

32 S. A. Tali, S. Soleimani-Amiri, Z. Sanaee and S. Mohajerzadeh, *Sci. Rep.*, 2017, **7**, 42425.

33 J. Bisquert and A. Compte, *J. Electroanal. Chem.*, 2001, **499**, 112–120.

34 BioLogic Science Instruments, *Ec-lab Software User's Manual Version 10.1x*, 2011.

35 B. H. Cipriano, A. K. Kota, A. L. Gershon, C. J. Laskowski, T. Kashiwagi, H. A. Bruck and S. R. Raghavan, *Polymer*, 2008, **49**, 4846–4851.

36 H. Deng, T. Skipa, R. Zhang, D. Lellinger, E. Bilotti, I. Alig and T. Peijs, *Polymer*, 2009, **50**, 3747–3754.